Dielectric and structural studies of $Ba_2MTi_2Nb_3O_{15}$ ($BMTNO_{15}$, $M=Bi^{3+},La^{3+},Nd^{3+},Sm^{3+},Gd^{3+}$) tetragonal tungsten bronze-structured ceramics

M. C. Stennett,[a] I. M. Reaney, G. C. Miles, D. I. Woodward, and A. R. West
Department of Engineering Materials, University of Sheffield, Sheffield S1 3JD, United Kingdom

C. A. Kirk
Mineralogy Department, Natural History Museum, London SW7 5BD, United Kingdom

I. Levin
Ceramics Division, National Institute of Standards and Technology, Gaithersburg, Maryland 20899

(Received 26 October 2005; accepted 26 March 2006; published online 29 May 2007)

The structure and dielectric properties of a new family of tetragonal tungsten bronze (TTB) ceramics with the general formula, $Ba_2MTi_2Nb_3O_{15}$ where $M=Bi^{3+},La^{3+},Nd^{3+},Sm^{3+},Gd^{3+}$, have been investigated. Hereafter the compositions will be referred to by the abbreviation $BMTNO_{15}$ where $M=B(Bi^{3+})$, $L(La^{3+})$, $N(Nd^{3+})$, $S(Sm^{3+})$ or $G(Gd^{3+})$. $BLTNO_{15}$ [permittivity maximum $(T_m)\sim -80\ ^\circ C$] and $BBTNO_{15}$ ($T_m\sim -100\ ^\circ C$) exhibited relaxorlike dielectric behavior. In contrast, $BNTNO_{15}$ ($T_m\sim 165\ ^\circ C$), $BSTNO_{15}$ ($T_m\sim 250\ ^\circ C$), and $BGTNO_{15}$ ($T_m\sim 320\ ^\circ C$) were classic ferroelectrics. T_m increased with decreasing radius of the M ion. Room temperature x-ray powder diffraction (XRD) patterns of all the compounds indexed on a prototype $P4/mbm$ (or $P4bm$) space group with lattice parameters $a\approx 12.4$ Å and $c\approx 4$ Å. However, electron diffraction revealed that the relaxor phases, $BLTNO_{15}$ and $BBTNO_{15}$, exhibited an incommensurate modulation, whereas the classic ferroelectric $BNTNO_{15}$, $BSTNO_{15}$, and $BGTNO_{15}$ featured an orthorhombic superstructure with lattice parameters $a\approx b\approx \sqrt{2}a_{TTB}$ and $c\approx 2c_{TTB}$. © *2007 American Institute of Physics*.
[DOI: 10.1063/1.2205720]

I. INTRODUCTION

Most of the known ferroelectric oxides crystallize with perovskite, tungsten bronze or pyrochlore structures. The majority of commercial ferroelectric ceramics are based on perovskites; the pyrochlores and tungsten bronzes have not been commercially exploited. Recently, Chen,[1] and Chen and Yang[2] reported the tungsten bronze (TTB) phases in the systems $BaO-RE_2O_3-TiO_2-Nb_2O_5$ (RE=rare earth) with high relative permittivity, ε_r (>100), and low dielectric losses, tan δ(<0.0003), in the radio frequency (rf) range. Kirk *et al.*[3] synthesized a single phase niobate composition with the stoichiometric formula, $Ba_2LaTi_2Nb_3O_{15}$. Reitveld refinement of XRD data confirmed the phase crystallized with a TTB structure (shown in Fig. 1) but was unable to distinguish between the noncentric space group $P4bm$ and the centrosymmetric space group $P4/mbm$. Cooling the sample from room temperature resulted in a frequency-dependent peak in the dielectric permittivity at approximately −80 °C. The permittivity maximum decreased in magnitude and increased in temperature with increasing frequency, which is typical for a ferroelectric relaxor. Miles *et al.*[4] determined the origin of this phase transition between the low temperature ferroelectric phase and the high temperature paraelectric phase, by variable temperatures powder neutron diffraction (ND) studies. Refinement of the data obtained above and below T_m showed that on cooling, the phase transition was associated with a lowering of symmetry from a centrosymmetric space group $P4/mbm$ to a noncentric space group $P4bm$. A number of phases with TTB structure have now been reported to exist, in which La has been replaced by other rare earth cations.[5] The present contribution reports on a systematic study of the crystal structures, microstructures, and electrical properties of dense $BMTNO_{15}$ ($M=Bi^{3+},La^{3+},Nd^{3+},Sm^{3+},Gd^{3+}$) ceramics.

II. EXPERIMENT

A. Powder preparation and characterization

The 100 g batches of stoichiometric compositions in the $BMTNO15$ ($M=Bi^{3+},La^{3+},Nd^{3+},Sm^{3+},Gd^{3+}$) systems were

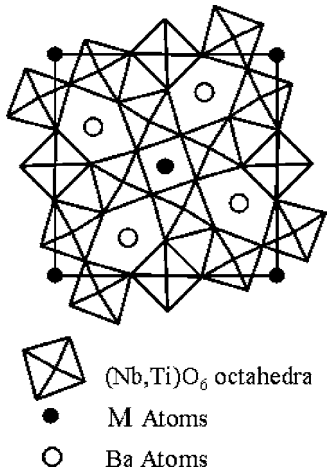

FIG. 1. Schematic of the TTB structure.

[a]Electronic mail: m.c.stennett@shef.ac.uk

produced by a conventional mixed-oxide processing route. The powder precursors were weighed out to four significant figures and attrition milled, using an Szegvari Attritor System Model 01-HD supplied by Union Process (Akron, USA), in a 750 ml mill pot (Tefzel-coated stainless steel) containing 1500 g of partially stabilized zirconia media (Y_2O_3) (3 mm) and 200 ml of isopropanol. A rotation speed of 300 rpm was used for 1 h and the slurry was separated from the media using a sieve and dried overnight at 100 °C. Once dry, the powder was sieved through a 200 μm mesh sieve and stored in a desiccator. The mixed powder batches were reacted at 1300 °C for 8 h in an open alumina crucible in air with the exception of the $M=Bi^{3+}$ composition, which was calcined at 1100 °C. The single-phase powders were then attrition milled for 1 h in an identical manner to the prereaction milling step except that after 45 min, 2 wt % polyethylene glycol (PEG) binder [molecular weight (MW)=10 000] was added to the slurry. Once the powder had been dried, 20 mm diameter pellets were pressed in a hardened stainless steel die using ~6 g of powder at a pressure of ~30 MPa. The pellets were sintered at 1150–1450 °C (3 °C min^{-1} ramp rate), depending on composition, in air for 4 h on a zirconia tile.

The phase purity of the powders was checked using a STOE STADI P diffractometer (Darmstadt, Germany) operated in transmission mode with a small position sensitive detector (PSD) and Ge monochromator. The diffractometer was operated at 40 kV and 40 mA using Cu $K\alpha$ radiation, $\lambda=1.541\,84$ Å. The scan range was between 8° and 70° 2θ with a step size of 0.01° 2θ and the count time was ~12 h. Samples were prepared by grinding the powder in a pestle and mortar with ethanol and applying to an acetate film which was loaded into the sample holder. A silicon standard was run prior to each measurement to allow calibration of the equipment. The peaks were indexed on a primitive tetragonal cell (space group $P4/mbm$ or $Pb4m$) and the lattice parameters were refined.

B. Microstructural analysis

A Cambridge CamScan II scanning electron microscope (Cambridge, USA) was used for microstructural analysis of the sintered pellets. Pellet fracture surfaces were thermally etched ~150 °C below their sintering temperature for 1 h in air to reveal the grain structure. The etched samples were cleaned ultrasonically in acetone and mounted onto aluminum stubs with Acheson Electrodag 1415M silver paint (Cannock, UK). Samples were then carbon sputter-coated using an Edwards "Speedivac" model 12E6/1598 (Crawley, UK) to prevent charging taking place in the microscope. Secondary electron images (SEIs) of the fracture surfaces were obtained at an accelerating voltage of 20 kV.

Transmission electron microscopy (TEM) was used to obtain more detailed structural and microstructural information. Samples for TEM were prepared from sintered pellets by conventional mechanical sectioning and grinding to a thickness of <30 μm. The thinning was completed in a Gatan dual ion beam mill (Pleasanton, USA) operated at 6 kV with a total specimen current of 0.6 mA and an incidence angle that varied between 10° and 15°. The samples were carbon coated to avoid charging using an Emitech k950 evaporation unit (Ashford, UK). Samples were examined in a Philips EM420T microscope (Eindhoven, Holland) operated at 120 kV. Kinematic electron diffraction patterns were simulated using the CARINE 3.1 software.

C. Electrical measurements

Dielectric measurements were conducted between 5 Hz and 1 MHz using an HP 4192A low frequency (LF) impedance analyzer connected to a conductivity jig. Pt electrode paste was painted onto opposite faces of the pellets, allowed to dry, and then fired at 900 °C for 1 h. The Pt electrodes were attached to the Pt leads of a two-terminal conductivity jig and temperature control was achieved by inserting the jig into a Carbolite tube furnace (Hope, UK). Low temperature measurements were obtained by placing the pellets into a compression-type jig and inserting into an Oxford Instruments cryostat (Oxford, UK). The data sets were processed and information extracted using the ZVIEW 2.1B analysis package. Dielectric measurements in the high frequency range (>1 MHz) were performed using a computer controlled high frequency dielectric spectrometer equipped with an HP 4291B impedance analyzer, a Novocontrol BDS2100 coaxial sample cell (Hundsangen, Germany), and a Sigma System M18 temperature chamber (San Diego, USA).

Ferroelectric *P-E* hysteresis loop measurements were performed using a Thurlby-Thandar TG1304 computer controlled function generator (Huntingdon, UK) in conjunction with a Chevin Research HVA1B high voltage amplifier (Otley, UK). A two-probe brass specimen holder was immersed in a temperature controlled silicon oil bath in order to obtain a stable (±0.5 °C) temperature environment for the experiments and also to help protect against dielectric breakdown across the edges of the samples. The induced current was converted to a measurable voltage signal by means of a custom-built *I-V* converter. Numerical integration of the measured current with respect to time yielded the polarization, thereby enabling determination of the *P-E* characteristics of the material.

III. RESULTS

A. Structural and microstructural characterizations

Figure 2 shows the room temperature XRD patterns of the fully reacted BMTNO$_{15}$ powders where $M=Bi^{3+}, La^{3+}, Nd^{3+}, Sm^{3+}, Gd^{3+}$. All patterns were indexed using the tetragonal space group $P4/mbm$ or $P4bm$. Fully indexed data for one phase, $M=Nd^{3+}$, have been reported previously.[5]

The refined lattice parameters as a function of the M ion size[6] are summarized in Fig. 3. The a lattice parameter decreased significantly with decreasing M size, whereas the c lattice parameter remained nearly unaffected.

Figure 4 shows the SEIs of etched fracture surfaces of the TTB samples. The amount of porosity in all samples appeared consistent with the measured densities (expressed as a percentage of the theoretical maximum).

Figure 5 shows the typical experimental and simulated (based on the ionic positions of Kirk *et al.*[3]) selected area

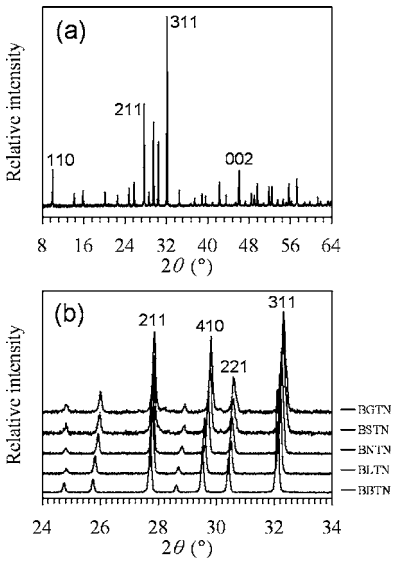

FIG. 2. (a) XRD pattern obtained from $BBTNO_{15}$ composition. All the reflections were attributed to a single TTB structured phase with space group $P4/mbm$ or $P4bm$. (b) Enlargement of region containing the major reflections. Patterns for all compositions overlaid for comparison. The major reflections have been indexed according to a TTB structure with space group $P4/mbm$ or $P4bm$.

electron diffraction patterns (SADPs) obtained along the $[001]_{TTB}$, $[100]_{TTB}$, and $[110]_{TTB}$ directions for $M=La^{3+}$ and Nd^{3+} samples. The fundamental reflections in all patterns could be indexed on the tetragonal cell $P4/mbm$, e.g., Figs. 5(a)–5(c). However, the $[100]_{TTB}$ pattern featured weak reflections at $0kl:k=2n+1$ which are forbidden in the $P4/mbm$ (or $P4bm$) space group, Figs. 5(d)–5(f). The $[110]_{TTB}$ pattern for $BLTNO_{15}$ exhibited incommensurate satellite reflections at $h(1/4+\delta)$, $k(1/4+\delta)$, $l/2$ where $\delta \approx 0.04$. For $\delta=0$, a commensurate superstructure could be observed with lattice parameters $a(\|[110]_{TTB})=\sqrt{2}a_{TTB}$, $b(\|[1-10]_{TTB})=2\sqrt{2}a_{TTB}$, and $c(\|[001]_{TTB})=2c_{TTB}$. In contrast to $BLTNO_{15}$, the $[110]_{TTB}$ pattern for $BNTNO_{15}$ featured commensurate superlattice reflections at $h/2$, $k/2$, $l/2$ positions corresponding to a unit cell with lattice parameters $a(\|[110]_{TTB}) \approx b(\|[1-10]_{TTB})=\sqrt{2}a_{TTB}$ and $c(\|[001]_{TTB})=2c_{TTB}$, Figs. 6(g)–6(i).

Dark-field imaging using the fundamental reflections in both $BBTNO_{15}$ and $BLTNO_{15}$, Figs. 6(a) and 6(b), respectively, showed no apparent domain structure. In contrast, dark-field imaging using fundamental reflections of $BNTNO_{15}$, $BSTNO_{15}$, and $BGTNO_{15}$, Figures 6(d)–6(f), respectively, revealed twin domains which could be attributed to a structural distortion away from tetragonal symmetry.

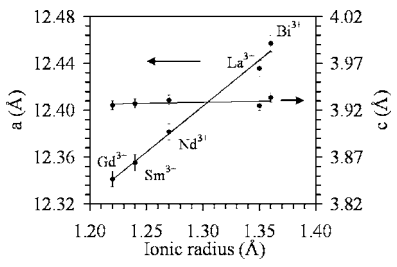

FIG. 3. Lattice parameters as a function of M ionic radius (Ref. 6).

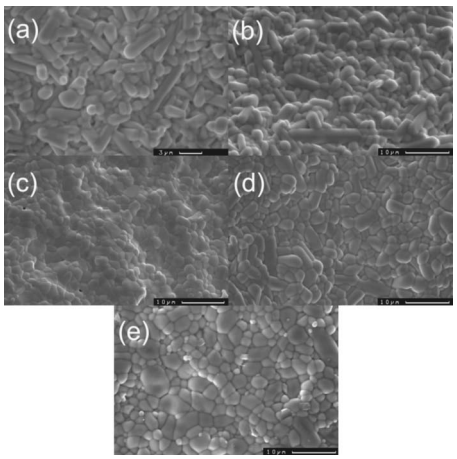

FIG. 4. Secondary electron images (SEIs) taken from (a) $BBTNO_{15}$, (b) $BLTNO_{15}$, (c) $BNTNO_{15}$, (d) $BSTNO_{15}$, and (e) $BGTNO_{15}$.

Dark-field imaging of $BNTNO_{15}$ using the $h/2$, $k/2$, $l/2$ superlattice reflections, which were most intense when oriented close to the $[114]_{TTB}$ zone axis orientation, revealed additional twinlike subdomains having bright and dark contrasts [strongest and arrowed in Fig. 7(b)].

B. Electrical characterization

Figure 8 shows the relative permittivity and dielectric loss as a function of temperature for $BMTNO_{15}$ ($M=Bi^{3+}, La^{3+}, Nd^{3+}, Sm^{3+}, Gd^{3+}$). For $BBTNO_{15}$ and $BLTNO_{15}$, the relative permittivity rose toward a maximum whose temperature was frequency dependent. As the maximum was approached from the low temperature side, the relative permittivity exhibited frequency dispersion. The dielectric loss also exhibited frequency dependence with the

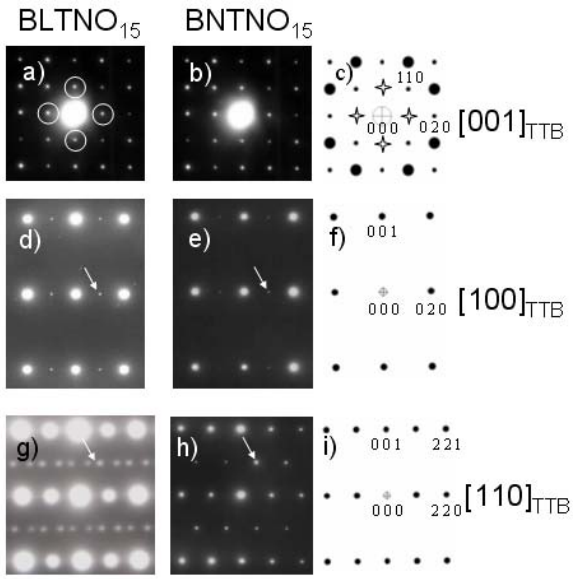

FIG. 5. [(a) and (b)] Experimental and (c) simulated $[001]_{TTB}$ [(d) and (e)] experimental and (f) simulated $[100]_{TTB}$, [(g) and (h)] experimental and (i) simulated $[110]_{TTB}$ SADPs obtained from $BLTNO_{15}$ and $BNTNO_{15}$. Simulations were obtained using space group $P4/mbm$ and atomic positions after Kirk *et al.* (Ref. 4) (Arrows indicate superlattice reflections and ☆ indicate spots arising from double diffraction.)

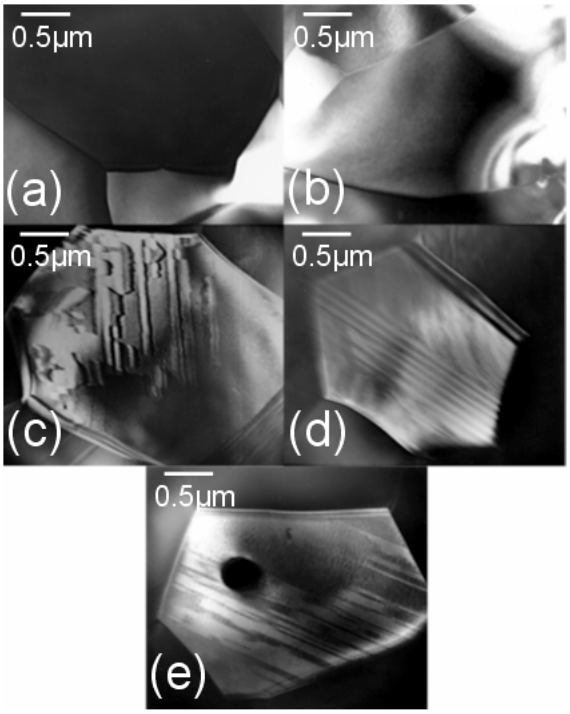

FIG. 6. General two beam diffraction contrast dark-field (DF) TEM images along the $[100]_{TTB}$ zone axis for (a) $BBTNO_{15}$, (b) $BLTNO_{15}$, (c) $BNTNO_{15}$, (d) $BSTNO_{15}$, and (e) $BGTNO_{15}$.

loss peak increasing in magnitude and shifting to higher temperatures with increasing frequency. This behavior indicated that the phase transitions were of the "relaxor" type characterized by a distinct shift in the relative permittivity maximum to higher temperatures with increasing frequency and an associated increase in the magnitude and temperature of the loss peaks.

For $BNTNO_{15}$, $BSTNO_{15}$, and $BGTNO_{15}$, Fig. 8, the relative permittivity increased to a frequency independent maximum. The dielectric loss was frequency-dependent at high temperature and exhibited a broad frequency-independent peak. From the dielectric data presented in Fig. 8, $BNTNO_{15}$, $BSTNO_{15}$, and $BGTNO_{15}$ appeared to exhibit classical ferroelectric rather than relaxor phase transitions.

The temperature of the relative permittivity maximum T_m increased with M ionic radius, Fig. 9. For completeness, data points have been included in Fig. 9 from two additional

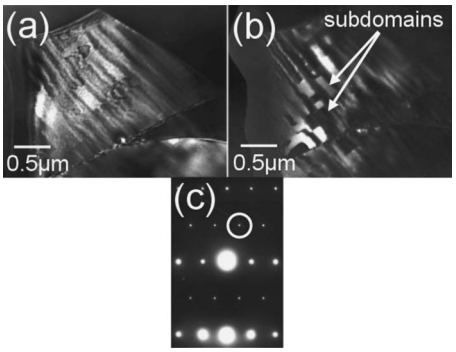

FIG. 7. DF TEM images obtained from $BNTNO_{15}$ recorded near the $[114]_{TTB}$ zone axis using (a) a fundamental reflection and (b) a superlattice reflection. (c) The $[114]_{TTB}$ SADP from $BNTNO_{15}$.

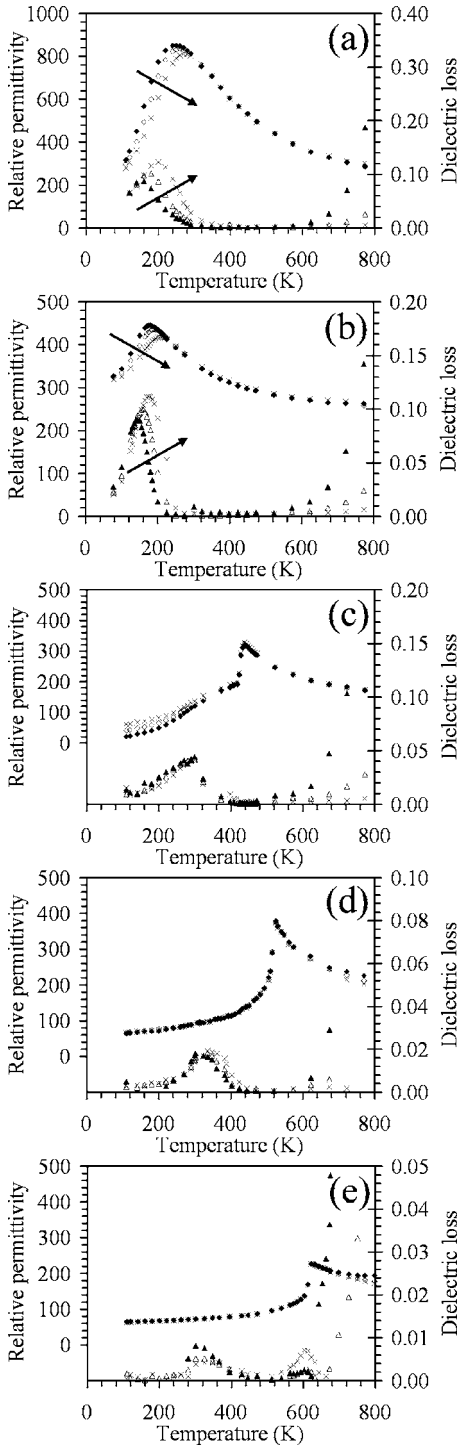

FIG. 8. Dielectric constant and dielectric loss as a function of temperature for (a) $BBTNO_{15}$, (b) $BLTNO_{15}$, (c) $BNTNO_{15}$, (d) $BSTNO_{15}$, and (e) $BGTNO_{15}$. The arrows, in (a) and (b), indicate the direction of increasing frequency.

TTB-structured compositions, $Ba_2EuTi_2Nb_3O_{15}$ ($BETNO_{15}$) and $Ba_2PrTi_2Nb_3O_{15}$ ($BPTNO_{15}$).[7] Although the general trends in relative permittivity as a function of temperature may be explained by either relaxor or ferroelectric behavior in these compounds, several additional anomalous frequency dispersions in the dielectric loss data were seen, the origin of which remains to be understood. $BNTNO_{15}$, $BSTNO_{15}$, and $BGTNO_{15}$ followed the Curie-Weiss law as expected for classical ferroelectrics, whereas both $BLTNO_{15}$ and

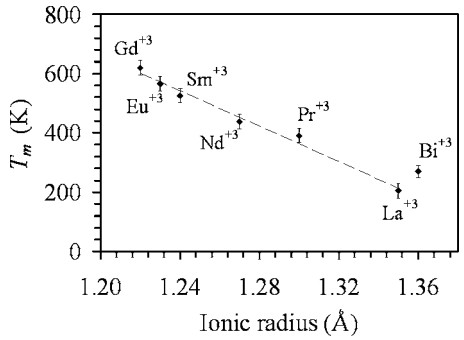

FIG. 9. T_m as a function of M ionic radius (Ref. 6); data points for Eu^{+3} and Pr^{+3} containing compositions after Pickthall *et al.* (Ref. 7).

$BBTNO_{15}$ exhibited deviations from Curie-Weiss behavior close to the relative permittivity maximum, similar to that reported for relaxors such as $Pb(Mg_{1/3}Nb_{2/3})O_3$ (PMN) and $Pb(Zr,Ti)O_3$ (PZN).[8]

Hysteresis measurements confirmed the ferroelectric nature of $BNTNO_{15}$, $BSTNO_{15}$, and $BGTNO_{15}$ ceramics. Figure 10 shows the behavior of $BNTNO_{15}$ above and below the relative permittivity maximum. Below, nonlinear hysteretic behavior, illustrating the reversibility of the polarization, was observed, characteristic of ferroelectric materials. Above, linear behavior was observed which indicated a paraelectric state. Similar hysteresis curves were obtained for $BSTNO_{15}$ and $BGTNO_{15}$.

Although some of the $BMTNO_{15}$ compositions investigated here exhibited reasonably low rf dielectric losses (~0.001), no microwave frequency resonance could be obtained using the cavity method. High frequency ($\geqslant$100 MHz) measurements were conducted on the $BLTNO_{15}$ samples to elucidate the reason for the lack of resonance. Figure 11 shows the real and imaginary parts, respectively, of the relative permittivity as a function of temperature and measurement frequency. rf measurements showed that $BLTNO_{15}$ exhibited relaxor-type behavior and displayed both an increase in the tan δ maximum and an upward shift in the temperature of the peak with increasing measurement frequency (Fig. 8). tan δ is related to the imaginary and real parts of the permittivity by the following equation:

$$\tan\delta = \frac{\varepsilon''}{\varepsilon'}.$$

The maximum values of ε'' and ε' decreased with increasing frequency in Fig. 11 but the peaks shifted upwards in temperature and the ε' and ε'' maxima occurred in the vicinity of room temperature at 1 GHz. Figure 12 illustrates the frequency dependence of tan δ. Although the maximum value of tan δ remained approximately the same for all frequencies, the loss peak shifted upwards and the maximum occurred at room temperature at 1 GHz. Since Q is inversely proportional to tan δ, this loss behavior explains the lack of measurable microwave resonance at room temperature for $BLTNO_{15}$. $BNTNO_{15}$ also exhibited frequency dispersion at low temperature in the rf data, Fig. 8, which may also be detrimental to MW properties.

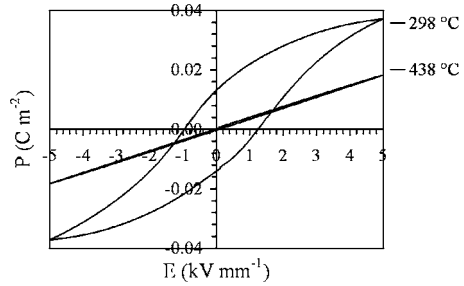

FIG. 10. Polarization (P) as a function of applied electric field (E) measured at 298 and 438 K for $BNTNO_{15}$.

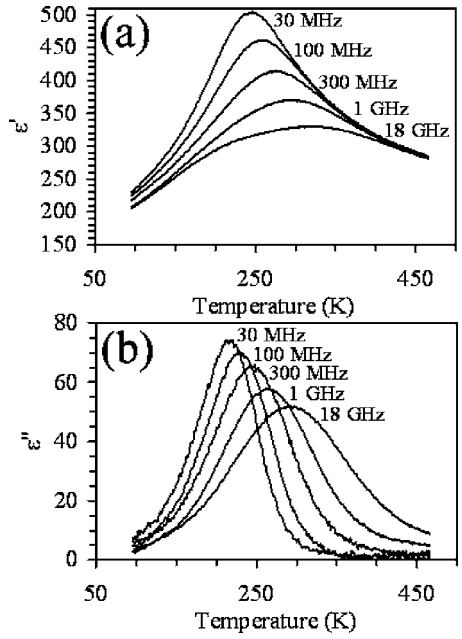

FIG. 11. (a) Real (ε') and (b) imaginary (ε'') part of the relative permittivity as a function of temperature and measurement frequency for $BLTNO_{15}$.

IV. DISCUSSION

Electron diffraction revealed the presence of extra reflections, in addition to the fundamental spots of the TTB structure, in all compositions. The extra reflections were shown to be incommensurate for $BBTNO_{15}$ and $BLTNO_{15}$ and commensurate for $BNTNO_{15}$, $BSTNO_{15}$, and $BGTNO_{15}$. This indicated a departure from the centrosymmetric $P4/mbm$ and noncentrosymmetric $P4bm$ space groups assigned to the phases based on the XRD (Ref. 3) and ND (Ref. 4) data. Many known tungsten bronze-structured compounds have been reported as having incommensurately modulated struc-

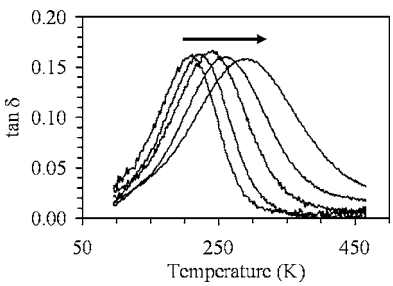

FIG. 12. tan δ as a function of temperature and measurement frequency for $BLTNO_{15}$. The arrow indicates the direction of increasing frequency.

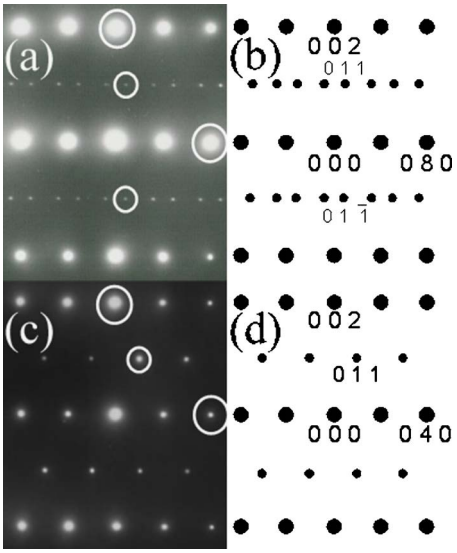

FIG. 13. (a) Experimental and (b) simulated $[100]_{Ama2}$ SADPs in $BLTNO_{15}$. (c) Experimental and (d) simulated $[100]_{Ima2}$ SADP's in $BNTNO_{15}$. Both directions are equivalent to the $[110]_{TTB}$ direction.

tures similar to that exhibited by $BMTNO_{15}$ ($M=La^{3+}$, Nd^{3+}), including $Ba_2NaNb_5O_{15}$ (BNN),[9] $Ba_xSr_{1-x}Nb_2O_6$ (BSN),[10,11] and $Pb_{1-x}Ba_xNb_2O_6$ (PBN).[12] The deviations from commensurate periodicity have been reported to be composition and temperature dependent. Bursill and Lin[10] and Grzinic[13] attributed the incommensurate modulation in BSN to an intergrowth of two different commensurate structures, designated as $R=1$ and 0. Both end-member structures were derived from the original TTB unit cell of BSN reported by Jamieson *et al.*[14] Bursill and Lin[10] proposed that the $R=1$ end member corresponded to a unit cell $a=17.58$ ($\sim\sqrt{2}a_{TTB}$), $b=35.16$($\sim 2\sqrt{2}a_{TTB}$), and $c=7.83$ Å($\sim 2c_{TTB}$) and this commensurate approximant had a space group *Ama*2.[15] The other end member ($R=0$) has been proposed to exhibit an orthorhombic unit cell $a_0 \approx 17.58(\sim\sqrt{2}a_{TTB})$, $b_0 \approx 17.58(\sim\sqrt{2}a_{TTB})$, and $c_0 \approx 7.83(\sim 2c_{TTB})$ with space group *Cmm*2, suggested but not refined by Jamieson *et al.*[14] and Lin and Bursill.[9] The most recent x-ray refinements of this incommensurate modulation using a super space group approach[16] questioned the validity of the intergrowth interpretation in favor of a harmonic modulation; however, the exact nature of modulation still remained elusive.

The experimental SADPs for $BMTNO_{15}$ ($M=Nd^{3+}$, Sm^{3+}, and Gd^{3+}) obtained in the present study are inconsistent with the *Cmm*2 space group suggested by Lin and Bursill.[9] Reconstruction of reciprocal lattice from a set of diffraction patterns for $BMTNO_{15}$ ($M=Nd^{3+}$, Sm^{3+}, and Gd^{3+}) suggested a body centered structure (possibly *Ima*2, a subgroup of *Cmm*2) with the lattice parameters $\sqrt{2}a_{TTB} \times \sqrt{2}a_{TTB} \times 2c_{TTB}$. Fig. 13 shows the diffraction patterns simulated for the $[100]_{Ama2}$ and $[100]_{Ima2}$ zone axes of the suggested $R=1$ and $R=0$ end members and the $\langle 110\rangle_{TTB} \| [100]_{Ama2} \| [100]_{Ima2}$-type patterns recorded for $BLTNO_{15}$ and $BNTNO_{15}$. The diffraction pattern for the $R=1$ end member, simulated based on the ionic positions reported by Labbe *et al.*,[15] contains rows of superlattice reflections [$\langle 011\rangle$ type in Figs. 13(a) and 13(b)] which occur near the $h+(1/4-\delta)$, $k+(1/4-\delta)$, $l+1/2$ positions of the incommensurate reflections observed for both $BBTNO_{15}$ and $BLTNO_{15}$. The $[100]_{Ima2}$ pattern from the $R=0$ end member, simulated based on the *Ima*2 cell, features systematic rows of commensurate reflections at $h+1/2$, $k+1/2$, $l+1/2$ which are similar to those observed experimentally for the [110] orientation of $BMTNO_{15}$ ($M=Nd^{3+}$, Sm^{3+} and Gd^{3+}), Figs. 13(c) and 13(d).

The combined electron diffraction dark field imaging and dielectric / hysteresis data indicate that $BMTNO_{15}$ ($M=Nd^{3+}$, Sm^{3+}, and Gd^{3+}) undergo, on cooling, cell multiplying and ferroelectric phase transitions which involve a change of crystal class. The inherent loss of symmetry elements upon these transitions between the prototype (high temperature) and room temperature structures is expected to generate orientational (non-180°), inversion (180°), and translational (antiphase) domains. Further work is necessary to clarify the details of the domain structures observed in Figs. 6 and 7.

Bi^{3+} and La^{3+} ions have approximately the same effective radius (~1.32–1.35 Å) (Ref. 6) for coordination number (CN)=12 with respect to O^{2-}. Nd^{3+}, Sm^{3+}, and Gd^{3+} ions (<1.27 Å) are all smaller. An overview of the literature concerning the crystal chemistry of TTB compounds suggests that all known phases that contain ions in the CN=12 (cuboctahedral) sites have radii larger than those of La^{3+} and Bi^{3+}, e.g., Na^{+} (~1.35 Å), Sr^{2+} (~1.44 Å), and Pb^{2+} (~1.49 Å).[9,10,12–16] To date, all compounds that have undergone electron diffraction analysis have been shown to exhibit an incommensurate modulation similar to that observed in $BBTNO_{15}$ and $BLTNO_{15}$. However, the commensurate, $R=0$ (*Ima*2), phase in $BMTNO_{15}$ ($M=Nd^{3+}$, Sm^{3+}, Gd^{3+}) has never previously been observed. The present study suggests that the $R=0$ commensurate TTB phase may be stable only for ionic radii $\leqslant \sim 1.30$ Å in CN=12 coordination.

$BLTNO_{15}$ and $BNTNO_{15}$ showed broad diffuse frequency-dependent peaks in their dielectric spectrum that suggested relaxor-type behavior, whereas $BNTNO_{15}$, $BSTNO_{15}$, and $BGTNO_{15}$ are ferroelectric at room temperature. Relaxors are unable to sustain a remnant polarization except at temperatures significantly below the temperature of maximum relative permittivity. The local symmetry of the system is lower than the global symmetry and the local chemistry is believed to prevent the establishment of normal long range polar ordering at T_m. Polar moments are, instead, established on the scale of the local chemistry.[17] The more complex dielectric behavior for relaxor ferroelectrics has been correlated to short range compositional or structural fluctuations by a number of authors.[18] The origin of the relaxor behavior is unknown but structural refinements[4] have indicated that the Nb^{5+} and Ti^{4+} ions are randomly distributed throughout the *B* sites which may contribute to the diffuse, frequency-dependent dielectric behavior.[18] The major structural difference between the compounds which exhibit relaxorlike behavior ($BLTNO_{15}$ and $BBTNO_{15}$) and those which are classic ferroelectrics ($BBTNO_{15}$, $BSTNO_{15}$, and $BGTNO_{15}$) is the presence of an incommensurate modulation in the former. The lack of commensurate periodicity may

contribute to the disruption of long range dipolar coupling in these compositions, resulting in relaxor rather than classic ferroelectric behavior.

V. CONCLUSIONS

TTB-structured compounds with the general formula, $Ba_2MTi_2Nb_3O_{15}$ ($M=Bi^{3+},La^{3+},Nd^{3+},Sm^{3+},Gd^{3+}$) formed within the $BaO-M_2O_3-TiO_2-Nb_2O_5$ systems. $BLTNO_{15}$ and $BBTNO_{15}$ exhibited relaxor behavior whereas $BNTNO_{15}$, $BSTNO_{15}$, and $BGTNO_{15}$ were first order ferroelectrics. The temperature of the relative permittivity maximum T_m increased as the radius of the M ion decreased. $BLTNO_{15}$ and $BBTNO_{15}$ exhibited incommensurate superlattice reflections at room temperature whereas $BNTNO_{15}$, $BSTNO_{15}$, and $BGTNO_{15}$ developed a commensurate superstructure.

ACKNOWLEDGMENTS

The authors would like to thank S. Kamba, at the Institute of Physics, Czech Academy of Science, Prague for the high frequency measurements (>1 MHz), D. Hall, at the Manchester Materials Science Centre, Manchester for the high field measurements and the Engineering and Physical Sciences Research Council (EPSRC) and Filtronic Comtek, PLC for financial support. One of the authors (I. L.) is grateful to the EPSRC-funded Ceramics and Composites Laboratory (CCL), Engineering Materials for their hospitality.

[1] X. M. Chen, J. Mater. Sci. **31**, 4853 (1996).
[2] X. M. Chen and J. S. Yang, J. Eur. Ceram. Soc. **19**, 139 (1999).
[3] C. A. Kirk, M. C. Stennett, I. M. Reaney, and A. R. West, J. Mater. Chem. **12**, 2609 (2002).
[4] G. C. Miles, M. C. Stennett, I. M. Reaney, and A. R. West, J. Mater. Chem. **15**, 798 (2005).
[5] G. C. Miles, M. C. Stennett, D. Pickthall, C. A. Kirk, I. M. Reaney, and A. R. West, Powder Diffr. **20**, 43 (2005).
[6] R. D. Shannon, Acta Crystallogr. **A32**, 751 (1976).
[7] D. Pickthall, G. C. Miles, and A. R. West (unpublished).
[8] G. Samara, J. Phys.: Condens. Matter **15**, R367 (2003).
[9] P. J. Lin and L. A. Bursill, Acta Crystallogr. **B43**, 504 (1987).
[10] L. A. Bursill and P. J. Lin, Acta Crystallogr. **B43**, 49 (1987).
[11] J. Schneck, J. C. Toledano, R. Whatmore, and F. W. Ainger, Ferroelectrics **36**, 327 (1981).
[12] C. A. Randall, R. Guo, A. S. Bhalla, and L. E. Cross, J. Mater. Res. **6**, 1720 (1991).
[13] G. Grzinic, Philos. Mag. **52**, 161 (1985).
[14] P. B. Jamieson, S. C. Abrahams, and J. L. Bernstein, J. Chem. Phys. **48**, 5048 (1968).
[15] Ph. Labbe, H. Leligny, B. Raveau, J. Schneck, and J. C. Toledano, J. Phys.: Condens. Matter **2**, 25 (1989).
[16] T. Woike *et al.*, Acta Crystallogr. **B59**, 28 (2003).
[17] D. Viehland, J. F. Li, S. J. Jang, L. E. Cross, and M. Wuttig, Phys. Rev. B **46**, 8013 (1992).
[18] R. E. Newnham and S. Trolier-McKinstry, in *Dielectric ceramics: Processing, Properties and Applications*, K. M. Nair, J. P. Guha, and A. Okamoto, (American Ceramic Society, Columbus, OH, 1993).